ACS APPLIED MATERIALS & INTERFACES

Research Article

www.acsami.org

Nanocomposite Coatings on Biomedical Grade Stainless Steel for Improved Corrosion Resistance and Biocompatibility

Srinivasan Nagarajan,[†,‡] Marimuthu Mohana,[†,§] Pitchaimuthu Sudhagar,[†,⊥] Vedarajan Raman,[#] Toshiyasu Nishimura,[‡] Sanghyo Kim,[§] Yong Soo Kang,[⊥] and Nallaiyan Rajendran*[,∥]

[‡]Structural Metals Center, National Institute for Material Science (NIMS), 1-2-1 Sengen, 305-0047 Tsukuba, Ibaraki, Japan

[§]Department of Bionanotechnology, Gachon University, Seongnam Si, Gyeonggi do 461 701, South Korea

[⊥]Energy Materials Laboratory, WCU Program Department of Energy Engineering, Hanyang University, Seoul 133-791, South Korea

[#]Japan Advanced Institute of Science and Technology, Japan 923-1292

[∥]Department of Chemistry, Anna University, Chennai 600025, India

Supporting Information

ABSTRACT: The 316 L stainless steel is one of the most commonly available commercial implant materials with a few limitations in its ease of biocompatibility and long-standing performance. Hence, porous TiO_2/ZrO_2 nanocomposite coated over 316 L stainless steels was studied for their enhanced performance in terms of its biocompatibility and corrosion resistance, following a sol–gel process via dip-coating technique. The surface composition and porosity texture was studied to be uniform on the substrate. Biocompatibility studies on the TiO_2/ZrO_2 nanocomposite coatings were investigated by placing the coated substrate in a simulated body fluid (SBF). The immersion procedure resulted in the complete coverage of the TiO_2/ZrO_2 nanocomposite (coated on the surface of 316 L stainless steel) with the growth of a one-dimensional (1D) rod-like carbonate-containing apatite. The TiO_2/ZrO_2 nanocomposite coated specimens showed a higher corrosion resistance in the SBF solution with an enhanced biocompatibility, surpassing the performance of the pure oxide coatings. The cell viability of TiO_2/ZrO_2 nanocomposite coated implant surface was examined under human dermal fibroblasts culture, and it was observed that the composite coating enhances the proliferation through effective cellular attachment compared to pristine 316 L SS surface.

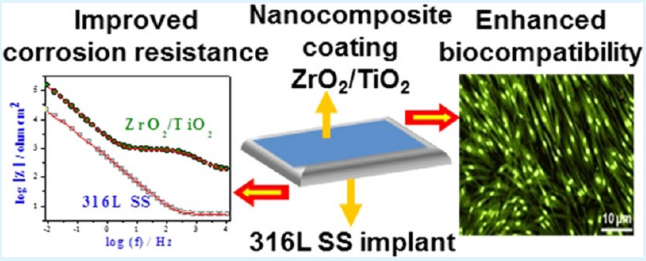

KEYWORDS: *TiO_2/ZrO_2 nanocomposite, sol–gel method, hydroxyapatite, simulated body fluid, corrosion resistance, biocompatibility*

1. INTRODUCTION

The type 316 L stainless steel is of great importance for the development of prosthetic materials in biomedical field, because of its lower cost, excellent fabrication properties, high corrosion resistance, and broader availability.[1] Stainless steel implants are often degraded because of pitting, crevice, and galvanic corrosion, which lead to the lowering of corrosion resistance and thereby affecting the mechanical stability of implant material and biocompatibility as well.[2] An ideal biomaterial is required to preserve its surface for an indefinite time sustaining vital properties such as biocompatibility and corrosion resistance. To retain surface of a biomaterial with its inherent properties for a long period of time, researchers have employed a variety of techniques to modify the surface of the implants. For instance, plasma spraying,[3] electrochemical deposition,[4] electrophoretic deposition,[5] pulsed laser deposition,[6] and biomimetic deposition[7] are a few of the techniques that have a wide acceptance commercially. However, the demerits with respect to each of the techniques still persists, like in the case of plasma spray deposition and pulsed laser deposition technique, which require a large amount of initial feed stock or target materials. In particular, the major limitation associated with pulsed laser deposition is the splashing or the particulates deposition on the film which lead to breakaway of surface defects under thermal shock.[8] Though coating methods such as electrochemical deposition (ECD) and electrophoretic deposition (EPD) are convenient for metal oxide coatings on metal implants during coating process, postsintering process at high temperature (450 °C) have shown to result in a detrimental effect on coating surface. In brief, in both ECD and EPD techniques either coarsening of grains or initiation of cracks have been reported to be observed oncoating surface due to the mismatch of thermal expansion coefficient between metal oxide coating and metal implants under high-temperature sintering process. These factors can affect the cell growth on metal implants.[9] Further, these cracks allow a direct contact between prosthesis and body fluid, which initiates localized corrosion at metal implant.[10] The entry of sol–gel technique has been

Received: May 6, 2012
Accepted: September 11, 2012
Published: September 11, 2012

considered as a boon in the field of coatings as it proved successful in terms of circumventing the above-mentioned demerits of other techniques. Inclusion of small amounts of organic additives while employing sol−gel method of coating often, supports the formation of crack-free film. Therefore, it has been anticipated that the issue of localized corrosion can be overcome by applying a sol−gel derived crack-free bioinert ceramic coating on the implant material. Consequently the passage of unwanted release of metal ions from the metal implant to body fluid is blocked.[11] Therefore, the sol−gel method has been proposed as a suitable procedure to produce protective[12] (relatively less crack) and bioactive[13] coatings at low cost. In addition, technological significance of these sol−gel coatings over to other methods have been widely documented.[14]

Recent approaches on TiO_2 thin film coated stainless steel implant have shown high biocompatibility in simulated body fluid (SBF). This property of TiO_2 can be attributed to the Ti−OH active groups present in the film inducing the ability of apatite formation on implant surface.[15−19] In addition, zirconium dioxide (ZrO_2) coatings have also shown higher potential for corrosion resistance because of their high wear resistance capacity without any chemical or biological bonding.[20,21] The past few years have seen a sharp increase in the interest for binary or mixed metal oxide systems and have been reported extensively for various catalytic applications because of their high surface area and acid base properties.[22,23] In particular, ZrO_2/TiO_2 (*ZT*) composite films have been of higher scientific and technological importance, due to its enhanced mechanical and thermal properties than their two individual participating components.[24] The ZT nanocomposite coatings have also been used in optical coatings owing to their good optical transparency and high refractive index.[25] The high photoactive nature of ZT composites have been reported to be highly advantageous in photocatalytic applications.[26] The benefits of *ZT* composite in in vitro cytotoxicity for biological application have also been reported.[27] However, there still is a scope for exploring mixed metal oxide coating on orthopedic implant. Development of a novel ceramic coating on implant material is attractive as it offers an enhanced osteointegration process along with faster bone regeneration. However, an implant material that is biocompatible with high corrosion resistance is scarce. In our earlier reports, were we had investigated the influence of porous morphology on apatite growth and corrosion resistance under SBF solution using TiO_2[28] and ZrO_2.[29] The results corroborated that apatite growth was highly supported by TiO_2 porous layer coating; unexpectedly it does not show remarkable corrosive resistance compared to porous ZrO_2 coatings. As similar, ZrO_2 coatings yielded high corrosion resistance with low apatite growth compared to that of TiO_2 coatings it is anticipated that composites of ZrO_2 and TiO_2 could synergistically offer both the biocompatibility and high corrosion resistance. In the present work, we attempt to improve the biocompatibility and corrosion resistance of 316 L SS implant by applying ZrO_2/TiO_2 (ZT) nanocomposite coatings. Further the apatite growth and cell viability test were demonstrated on ZT nanocomposite covered 316 L SS metal implants to elucidate the biocompatibility property. In addition, the ZT nanocomposite coating was investigated for its corrosion protective behavior over 316 L SS implant material.

2. EXPERIMENTAL TECHNIQUES

2.1. Synthesis of ZT Composite Coatings. Titanium(IV) isopropoxide (TIP) (Sigma-Aldrich) and zirconium propoxide (ZrP) (Sigma- Aldrich), were used as precursors of TiO_2 and ZrO_2 respectively. Triethanolamine (TEA) (Alfaacer), ethanol (EtOH) (Merck) and polyethylene glycol (PEG) (M_w: 600, Merck) were used as-received without any further purification. Typical one pot synthesis of sol−gel derived (1:1) *ZT* nanocomposite sol was as follows; the relative volume ratio of each of the precursors were 1.5: 1.5: 1: 20: 0.5 (TIP: ZrP: TEA: EtOH: PEG) and these were taken in beakers and were stirred for 30 min until the formation of a homogeneous sol. Following which, the mechanically polished 316 L SS electrodes (composition given in Table 1) of size 10 × 20 × 2 mm^3 were dipped in the homogeneous sol and was pulled out with a indigenously made microprocessor controlled dip coater at a withdrawal speed of 1 cm/min. The composite film coating procedure was repeated three times to ensure a homogeneous film formation on implant surface. The sol−gel *ZT* composite coating obtained on surgical grade 316 L SS was subsequently dried and sintered at 500 °C for an hour in air atmosphere. The adhesion of ZT films on metal implant was tested by ASTM D 3359 cross-cut tape-test (B).

Table 1. Elemental Composition of 316L SS Metal Implant

	main alloying elements (wt %)					
alloy	Cr	Ni	Mo	N	C	Mn
316 L SS	17.20	12.60	2.40	0.02	0.03	1.95

2.2. Physical Characterization. X-ray diffraction patterns were recorded with a PanAnalytical X-pert pro diffractometer using Cu Kα radiation, with 40 KV and 30 mA, at a scan rate of (2θ) 0.02°. The XRD pattern of *ZT* composite film was indexed based on the standard JCPDS (Joint Committee on Powder Diffraction Standards) files corresponding to TiO_2 and ZrO_2. The chemical compositions of the *ZT* coatings were studied by X-ray photoelectron spectroscopy (XPS) (VG Microtech −UK, Model VG Multilab ESCA 2000). The binding energies obtained in the XPS analysis were corrected taking into account the specimen charging and by referring to C 1s at 284.60 eV. The structure and morphology of the obtained nanocomposite were characterized using scanning transmission electron microscopy (STEM; JEOL JEM-2100F, 200 kV) and by scanning electron microscopy (SEM) on a Hitachi Model-S 3400. The surface topography measurement was performed using atomic force microscopy (AFM) (Nanosurf AG, Grammetstrasse 14, CH-4410 Liestal, Switzerland) instrument. All the images were recorded under air atmosphere at room temperature. The FTIR spectra were recorded in the range of 400−4000 cm^{-1} using Thermo Electron Corporation, USA.

2.3. Electrochemical Analysis. A conventional three electrode cell was used for all the electrochemical measurements. A saturated calomel electrode (SCE), platinum foil and the test material was used as a reference electrode, counter electrode and working electrode, respectively. The simulated body fluid (SBF) solution was used as the electrolyte during the electrochemical immersion test.[30] The simulated body fluid (SBF) was prepared by the according to a procedure reported elsewhere.[27] The potentiostat (model PGSTAT 12, AUTOLAB, The Netherlands B.V.) was controlled by a personal computer and the software (GPES Version 6.0) for conducting the potentiodynamic polarization measurements. The potential was applied to the working electrode at a scan rate of 1 mVs^{-1} from cathodic to anodic direction. The corrosion rate was estimated using Tafel plot method.[31]The electrochemical impedance measurements were carried out using a frequency response analyzer (FRA) (Potentiostat model PGSTAT 12). Impedance spectra were acquired in the frequency range of 40 kHz−0.01 Hz with a 10 mV amplitude sine wave generated by the FRA. The bare and *ZT* coated 316 L SS metal implants were immersed at SBF solution for 7 days. For elucidating the time dependent properties, the electrochemical studies

(potentiodynamic polarization and impedance) were measured immediately after immersion and after 7 days.

2.4. Live/Dead Staining and In Vitro Cell Viability Assay. Human dermal fibroblasts (HDFn) were cultured in supplemented medium 106 (Invitrogen) with 1% penicillin-streptomycin. Cells were detached from culture flask using trypsin/EDTA, washed and counted using hemocytometer (Marienfeld Laboratory Glassware,Germany) prior to the biocompatibility analysis. Bare and *ZT* nanocomposite coated 316 L SS were kept in 6 well plates and UV sterilized for 30 min. HDFn cells with a density of 2×10^5 cells/ml were seeded in each well containing sterile samples and incubated at 37 °C with humidified 5% CO_2 environment. From live/dead staining dye kit (Biovision), 1 μL each of dye mixtures A (Live-Dye, a cell-permeable green fluorescent dye (Ex/Em = 488/518 nm) and B (propidium iodide (PI), a cell nonpermeable red fluorescent dye (Ex/Em = 488/615) were diluted in 1000 μL of dilution buffer (followed the manufacturer's protocol). On fifth day of culture, culture medium was removed and the previously prepared staining solution was added to the samples and incubated for 15 min at 37 °C. The stained samples were examined under fluorescence microscope using a filter which detects FITC and rhodamine. Biocompatibility of *ZT* nanocomposite coated 316 L SS was elucidated using cell proliferation reagent WST-1 test kit (Roche). On the third and fifth days of the culture period, the medium was removed and the specimens were transferred to another 6 well plates. WST-1 reagent and medium were diluted in 1:10 ratio and added to 6 well plates containing samples and incubated for 4 h at 37 °C. Supernatants were analyzed using a microtiter plate reader at 450 nm with a reference wavelength of 625 nm (PerkinElmer VICTOR 3 microplate reader (Waltham, MA, USA). Experiments were conducted in triplicate and statistical significance of $p < 0.05$ was analyzed using one way analysis of variance ANOVA.

3. RESULTS AND DISCUSSION

3.1. Surface Composition, Morphology and Adhesion. The X-ray diffraction pattern of *ZT* composite coating on 316 L SS film is shown in Figure 1. The X-ray diffractogram indicated

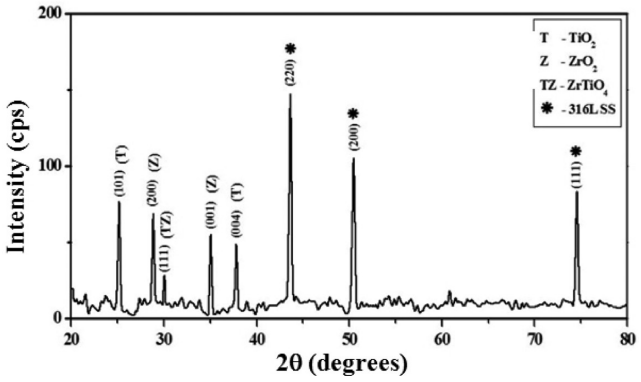

Figure 1. X-ray diffraction pattern of ZT nanocomposite coated on 316 L SS.

a pure composite coating over the stainless steel substrate. A mixture of characteristic peaks at the 2θ values of 25.4° and 37.8° corresponds to planes (101) and (004), respectively of anatase titanium dioxide (JCPDS No. 21−1272). The monoclinic zirconia phases (JCPDS No. 37−1784) were identified at 28.1° and 35.2°, corresponding to the planes of (200) and (001), respectively. The observed peak at $2\theta = 30.1°$, revealed the presence of zirconium titanate ($ZrTiO_4$) phase (JCPDS No. 80−1783). These characteristic peaks of each oxide apparently deciphered the presence of TiO_2, ZrO_2 and $TiZrO_4$ along with stainless steel substrate. The strong signals observed at $2\theta = 43.5$, 50.7, and 74.6° corresponds to the cubic centric $Cr_{0.19}$ $Fe_{0.7}Ni_{0.11}$ from the stainless steel substrate were with a crystallite orientation along (220), (200), and (111), respectively.[32]

Further, the chemical composition of *ZT* nanocompositie coatings were confirmed by using X-ray photoelectron spectroscopy and the resultant Ti2p, Zr3d and O1s core spectra are given in Figure 2. the Ti2p core XPS spectrum

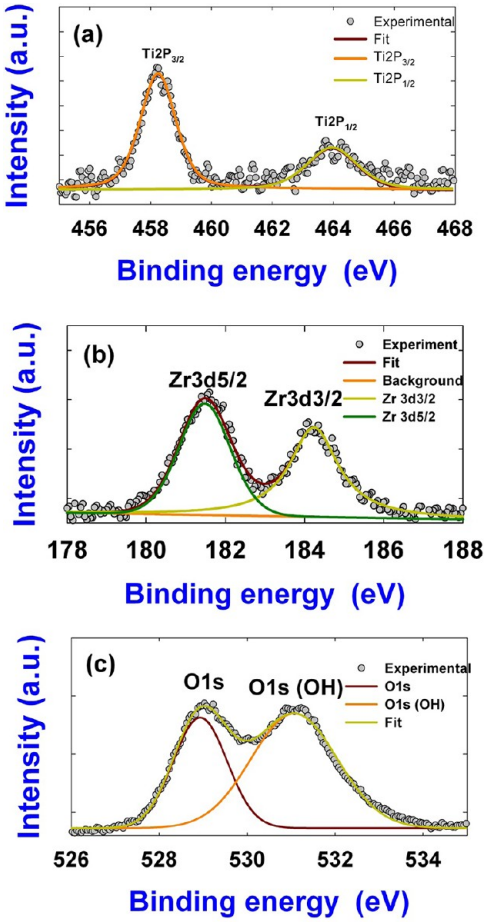

Figure 2. X-ray photoelectron spectra of ZT nanocomposite coated 316 L SS implant; XPS scan profile of (a) Ti 2p, (b) Zr 3d, and (c) O 1s core spectra.

shown in Figure 2b exhibits the characteristics peaks of $Ti2p_{3/2}$ − $Ti2p_{1/2}$ with typical doublets at 457.7 and 463.5 eV, respectively. The peak observed at ~458 eV corresponds to the reported value for Ti−O bonding. As shown in Figure 2b, the two peaks at 181.5 and 184.1 eV, corresponds to $Zr3d_{5/2}$ and $Zr3d3_{/2}$, respectively.[33] In both cases, the shape of the spectra and the position of the peaks (binding energies) clearly indicate the formation of TiO_2 and ZrO_2 by the dip-coating method used in the present investigation. The O1s core spectra (Figure 2c) were fitted with two asymmetric Gaussian curves and found to be fitting well with the experimental data. The Gaussian curve at 529.7 eV represents lattice oxygen in mixed metal oxide M−O (M = Zr and Ti), and the shoulder at 531.8 eV corresponds to surface hydroxyl oxygen in O−OH. TEM analyses were carried out in order to understand the microstructure of the ZT nanocomposite and the elemental distribution in the coating. Figure 3 shows the energy dispersive spectroscopy (EDS) results of the *ZT* nanocomposite film. As seen from the figure, the EDS mapping clearly evinces the

dx.doi.org/10.1021/am301559r | ACS Appl. Mater. Interfaces 2012, 4, 5134−5141

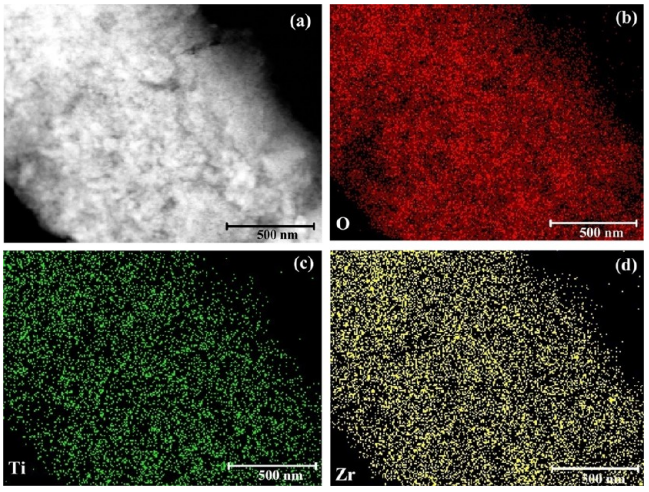

Figure 3. (a) STEM image of ZT nanocomposite and (b–d) STEM mapping images of ZrO_2–TiO_2 nanocomposite.

uniform distribution of titanium and zirconium in *ZT* composite coating.

The ability of adhesion offered by the *ZT* composite coating over the 316 L SS implant was tested by ASTM D 3359 cross-cut tape-test (B). The strength of adhesion was conferred to be good. Absence of any visual peel-off in the coating on the coated surface of the implant material and the fact that no *ZT* nanocomposite was found on the adhesive surface of the tape after the test confirmed the good ability of adhesion by the coating.. The adhesion was classified into category ASTM class 4B for *ZT* composite coated 316 L SS. Figure 4a shows the topographic AFM image of *ZT* composite coated on 316 L SS. The image clearly demonstrates the uniform and porous nature of the coating. Figure 4b illustrates the line profile images of the *ZT* composite coating. The crests in the profile represent the

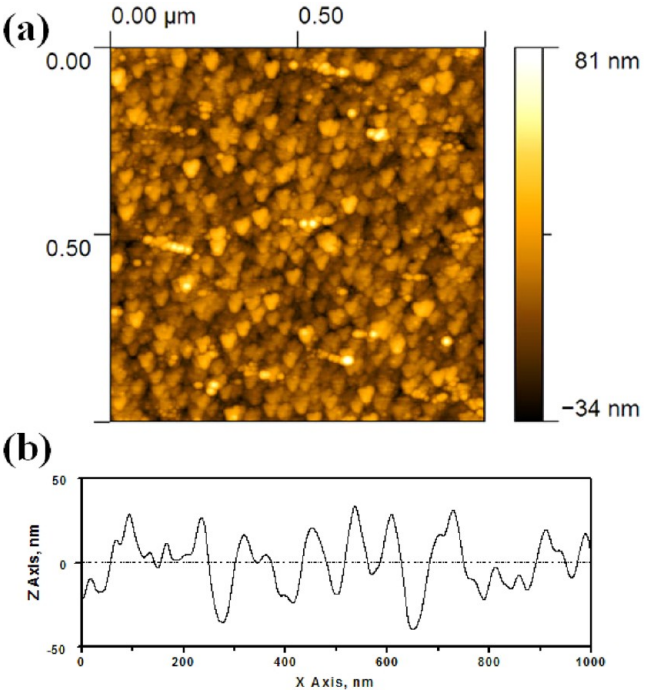

Figure 4. AFM image of ZT coated on 316 L SS: (a) topographic image, (b) line profile from section analysis.

dimensions of the crystallite growth and the troughs indicate the availability of pores in the coatings. The profile also evinces a continuous *ZT* composite coating with a peak-to-peak height of 25–50 nm in *z* axis, which indicates a highly porous surface. The dimension of shallow pores were estimated from AFM line (distance between two adjusting peak in the line profile) and found to be in the range between several tens of nm to 100 nm in diameter. The particle size from the line profile was found to be around 35 to 75 nm. It is generally thought that the crystallites growth can be attributed to the increase in strain resulting from the substitution of Ti^{4+} ions with Zr^{4+}, lowering the driving force for the crystallite growth.[34] However, the porous surface initiate the bonelike apatite layer uniformly along its surface. Kim et al.[35] demonstrated that the porous surface encouraged bone ingrowth over the porous structure, thereby providing a strong morphological fixation of the implants to bone.

Panels a and b in Figure 5 show the infrared spectra of *ZT* coated 316 L SS and apatite grown over *ZT* coated 316 L SS,

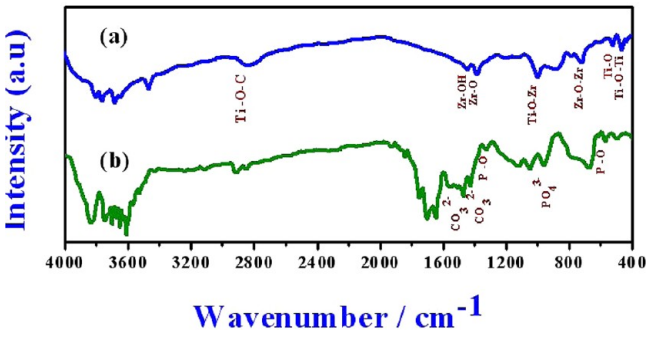

Figure 5. FTIR spectra of ZT coated 316 L SS (a) before immersion in SBF solution and (b) after immersion in SBF solution (for 7 days).

respectively. From Figure 5a, *ZT* coated 316 L SS showed refelectance peaks at 466, 511, and 2880 cm^{-1} which can be attributed to the presence of Ti–O–Ti, Ti–O, and Ti–C, respectively.[28] In addition, the peaks observed at 710, 1385, and 1453 cm^{-1} evinced the presence of Zr–O–Zr, Zr–O, and Zr–OH modes of vibration.[29] A unique and distinct peak at 1000 cm^{-1} clearly demonstrated the formation of metal oxide composite (Ti–O–Zr bonding). The result was in accordance with the XRD and XPS results. The peaks in the range of 3000–3800 cm^{-1} can be attributed to the presence of OH groups in the *ZT* composite film.

The hydroxyapatite (HAp) grown over 316 L SS coated with *ZT* composite (Figure 5b) exhibited refelectance peaks at 571, 602, and 1036 cm^{-1} suggesting the formation of PO_4^{3-} species groups on implant surface. Further, stretching vibration for PO_4^{3-} group from HAp was obtained at 1318 cm^{-1} for P–O stretch and 571 cm^{-1} for P–O stretch coupled with P–O bend.[36] The sharper peak for HAp bands pertaining to CO_3^{2-} group from carbonate substituted OH and PO_4^{3-} groups in HAp were obtained at about 1420 and 1460 cm^{-1}. The presence of carbonate peak in the FT-IR spectrum claimed the formation of carbonated hydroxyapatite. The identified finger-print feature of HAP was in line with our earlier report on individual metal oxide coated implant materials (TiO_2 and ZrO_2)[28,29] as well as other reports on HAP.[37] The above results unambiguously proved that *ZT* nanocomposite surface show comparatively high bioactivity than that of individual metal

dx.doi.org/10.1021/am301559r | ACS Appl. Mater. Interfaces 2012, 4, 5134–5141

oxide coatings. The possible reason for this trend will be discussed in the following section.

Typical surface morphology of *ZT* composite coated 316 L SS is presented in Figure 6a. Figure 6a apparently exhibits the

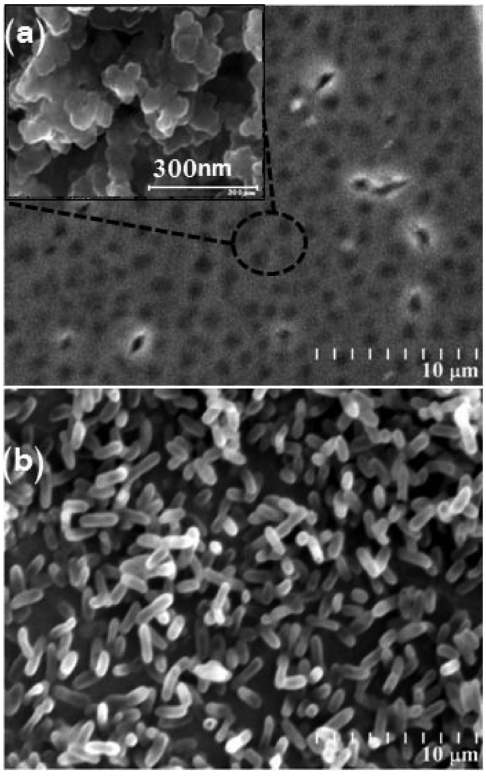

Figure 6. (a) SEM images of bare ZT coated 316 L SS surface and (b) 1D hydroxy apatite growth.

porous morphology on the coated surface of 316 L SS. These observed pore architecture affords advantage over the conventional compact surfaces. The porous surface enhances the mediation between simulated body fluid and inner pores of *ZT* composite coating due to high capillary force maintained along the pore walls. This argument is testified with surface wettability test. The contact angle measurements were performed on pristine and *ZT* composite coated 316 L SS metal implants (see the Supporting Information, Figure S3) and found to be *ZT* coated metal implant surface have high wettability (θ = 34.4°) than the pristine surface(θ = 75.4°). This implies that *ZT* surface coating on SS implant improve the hydrophilicity of bare 316 L SS implant, and the enhanced hydrophilicity is consistent with HAp formation on metal implant surface. In addition, the presence of abundant hydroxyl group exisisting in the pores also highly supporting the HAp growth.[38,39]

The morphology of hydroxyapatite growth on *ZT* composite coated surface is presented in Figure 6 (b). It reveals the formation of rod shaped hydroxyapatite with the average length in the dimensions of 1 to 3 μm (aspect ratio ~10). The possible reason of an nonproportional, single-axis elongated, 1D (one-dimensional) rodlike apatite crystals formation can be attributed to the high concentration of Ca^{2+} along a one direction. In principle, apatite growth is initiated by consuming the calcium and phosphate ion in the SBF solution. In this case, the development of a high concentration of Ca^{2+} along one direction leads to oriented aggregation and fusion of primary crystalline domains. A similar observation has been made by Mcquire et al.[40] According to their report, the growth of HAP specifically along the *c*-axis direction has been attributed to the inhibition of the random direction growth by the highly positively charged polarities. The results in primary crystallites (seeds) with relatively small domain size and low surface charge that rapidly aggregated unidimensionally to produce highly elongated 1D nanorods.[41]

In the case of uncoated 316 L SS there is no appriciable HAp growth (Supporting Information Figure S1) may be atrributed to the weak bioactivity of uncoated 316 L SS metal surface. This results endorsed that *ZT* nanocomposite coated metal surface showed high bioactive characteristics. The energy dispersive analysis spectra of the *ZT* composite coated 316 L SS metal implant exhibits (see the Supporting Information, Figure S2a) the Kα value of 4.5 and 2.1 is corresponding to Ti and Zr elements and the observed Ca and P element (see the Supporting Information, Figure S2b) confirms the apatite formation.

3.2. Electrochemical Analysis. The potentiodynamic cyclic polarization curves of uncoated and *ZT* composite coated 316 L SS is presented in Figure 7. From Figure 7, the

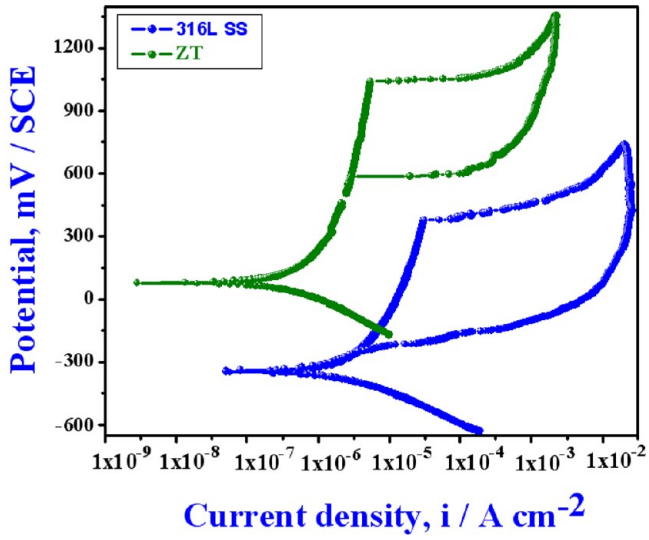

Figure 7. Potentiodynamic cyclic polarization curves of pristine and *ZT* coated 316 L SS in SBF solution. [Note that of polarization measurement scanning is start from cathodic to anodic direction].

ZT coated 316 L SS implant material showed a decrease in the passive current density (0.25 μA/cm^{-2}), i.e., the current density at which the metal remains passive. A distinct positive break down potential shift (663 mV) was observed in *ZT* coated metal implants compare to uncoated sample. This potential shift indicates that the *ZT* coating act as a geometric blocking layer against exposure to corrosive medium.[42] In general, the area of hysteresis loop in potentiodynamic cyclic polarization curve directly provides the information about degree of localized corrosion. For instance, a large area of hysteresis loop indicates a higher susceptibility of the material toward corrosion. In the present work, the area of hysteresis loop in uncoated metal implants was observed to be higher compared to *ZT* coated sample. This comparison revealed that the *ZT* coating act as barrier to preclude the physical contact between the electrolyte and metal implant surface, consequently corrosion resistance of the metal implants has improved.

Furthermore, the corrosion rate has been evaluated using Tafel plot method. From Tafel analysis uncoated implants showed high corrosion rate of 1.2×10^{-2} mmpy, and found to be markedly lowered about 1.6×10^{-3} mmpy under ZT composite. Therefore, it is expected that the release of metal ions or particles from the 316 L SS implant surface may effectively blocked by *ZT* composite coating which prevent the inflammation reaction with the surrounding tissues.

The electrochemical impedance results (Bode phase angle and resistance plots) of bare and *ZT* composite coated 316 L SS immersed in SBF solution are presented in Figure 8. In

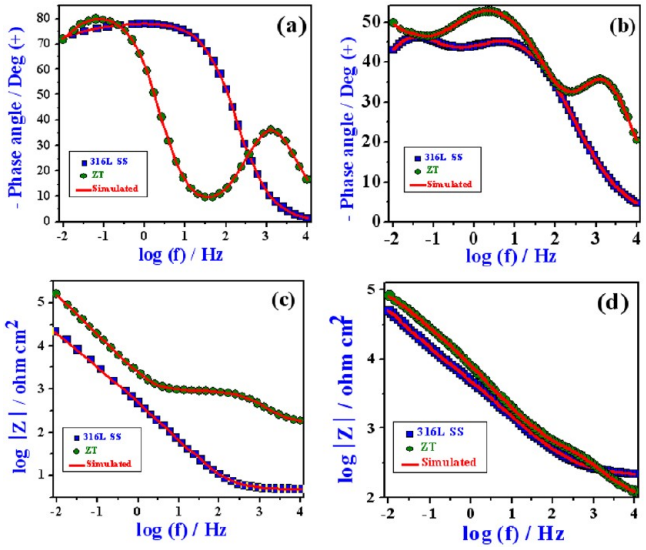

Figure 8. (a, b) Bode phase angle plots of uncoated and ZT coated 316 L SS implants; (c, d) Bode resistance plots of uncoated and ZT coated 316 L SS implants (Note that a and c samples were instantaneously measured under SBF solution; b and d samples were measured after 7 days immersed in SBF solution).

Figure 8a, the Bode phase angle plot of *ZT* coated samples exhibit an additional time constant at −35° compared to the uncoated 316 L SS in SBF solution, immediately after immersion (0 day). We presumed this additional shoulder might correspond to the presence of a blocking layer in the form of *ZT* coating on 316 L SS metal surface. Figure 8b represents the Bode plots measured after 7 days of immersion in SBF solution. It can be observed that *ZT* coated samples have a distinct time constant at 55°, which can be ascribed to the HAp formation and an inexplicit time constant in the uncoated metal implant reveals the poor or absence of any HAp growth. Though Bode phase angle plots primarily confirm the material interfaces (*ZT* and HAp) it needs further understanding to define the interrelationship between the interfaces and corrosion resistance.

To gain further insight into the corrosion resistance changes on uncoated and *ZT* coated metal implant under SBF solution the impedance results were analyzed with equivalent circuit model[43] (see the Supporting Information, Figure S4). The fitting results were embedded with experimental data in Figure 8, and is found that fitting results were excellent agreement with experimental data. The corresponding equivalent circuits are presented in Figure S3 (see the Supporting Information) and fitted values are enlisted in Table 2. From the Table 2, electric double layer capacitance value of *ZT* coated implant can be found to be one order (Q_b ~14.8 μF cm^{-2}) lower than

Table 2. Impedance Parameters of Bare and ZT Coated 316L SS in SBF Solution (immersed 0 days)

R_s (Ω cm^2)	Q_c (μF cm^{-2})	n_c	R_c (kΩ cm^2)	Q_b (μF cm^{-2})	n_b	R_b (kΩ cm^2)
216[a]				26.83	0.77	76
160[b]	0.02	0.63	362	14.80	0.85	235

[a]Bare 316 L SS. [b]TiO_2/ZrO_2 coated 316 L SS (Q_c charge accumulation)

uncoated implants (Q_b~ 26.8 μF cm^{-2}). The lower resistance explains the obstruction of charge accumulation at metal implant/SBF solution by *ZT* coating. As a result, the metal implant exhibits higher corrosion resistance about 362 kΩ cm^2 under *ZT* coating, which implies an efficient blocking of the passage of ions from the SBF solution to implant surface. In Table 3, *n* value directly correlates the homogeneity of surface ($n \leq 1$). Comparing *n* values of pristine 316 L SS (n_b = 0.77) and *ZT* composite coated 316 L SS (n_c = 0.63), the low value of *n* at *ZT* composite indicates that the surface contains pores and are in good accordance with AFM and SEM results.

From Table 3, the HAp growth can be examined in view of double layer capacitance values. For instance, highly dense HAp growth at metal implant results in high charge accumulation. Here, *ZT* coated implant reveal high charge accumulation posing a value of about *Qc* ~0.41 μFcm^{-2} compared to the uncoated implant Q_c ~0.04 μF cm^{-2}. This explicitly implies the charge transfer/ion exchange at the interface on the *ZT* coated implant implicating an effective HAP growth. This results are in good agreement with our earlier disscussions. Furthermore, the corrosion resistance R_a of *ZT* coated implant showed high values (56.80 kΩ cm^2) than that of uncoated implant (5.5 kΩ cm^2). This strongly endorse that *ZT* coated implant affords effective hydroxyapatite growth, which obviously supply resistance to the implant material. On the other hand the resistance of implant material R_c remains unchanged (~182 kΩ cm^2) even after an immersion period of 7 days in SBF solution.

3.3. Live/dead staining and in vitro cell viability assay.

Live/dead staining test helps in optically visualizing the viability of HDFn cells on bioimplant material 316 L SS with and without *ZT* nanocomposite coating. The test was carried out for 5 days continuously. Representative images corresponding to day 3 and day 5 are produced in this article. Green and red fluorescence corresponding to live and dead cells respectively, where obtained from the dye components calcein-AM for green and ethidium homodimer-1 for red. Figure 9 shows the differently magnified fluorescent images of cells grown on 316 L SS (Figure 9a, b) and *ZT* nanocomposite coated 316 L SS (Figure 9c, d) at fifth day culture. The cellular attachment, spreading and proliferation with highly elongated morphology was obtained for *ZT* coated sample (Figure 9c and d). Whereas, the reference 316 L SS material shows less cellular confluency even after 5 days of culture. Qualitatively determined results coincided well with quantitative WST-1 cell proliferation assay results (Figure 9e). The absorbance shown can be directly related to the viability of cells. A statistically significant ($p < 0.05$) difference in HDFn cells' proliferation between uncoated 316 L SS and *ZT* coated 316 L SS samples was observed both on day 3 and day 5. The graph demonstrates the near-stoppage of HDFn cells' proliferation on 316 L SS material as early as on day 3. No significant increase in cell density was observed after day 3. Evenmore, the cell viability for 316 L SS material was significantly lesser than that of cells grown on *ZT* coated

dx.doi.org/10.1021/am301559r | ACS Appl. Mater. Interfaces 2012, 4, 5134−5141

Table 3. Impedance Parameters for Bare and ZT Coated 316L SS in SBF Solution (immersed for 7 days)[a]

R_s (Ω cm^2)	Q_a (μF cm^{-2})	n_a	R_a (kΩ cm^2)	Q_c (μF cm^{-2})	n_c	R_c (kΩ cm^2)	Q_b (μF cm^{-2})	n_b	R_b (kΩ cm^2)
206[b]	0.09	0.87	5.5				11.4	0.65	182
95[c]	0.41	0.80	56.8	0.06	0.68	417	7.0	0.44	188

[a] R_a, impedance at hydroxyapatite/SBF solution interface; R_c, impedance at ZT coating/SBF solution interface; R_b, impedance at implant metal/SBF solution interface; Q, charge accumulation. [b]Bare 316 L SS. [c]ZT coated 316 L SS.

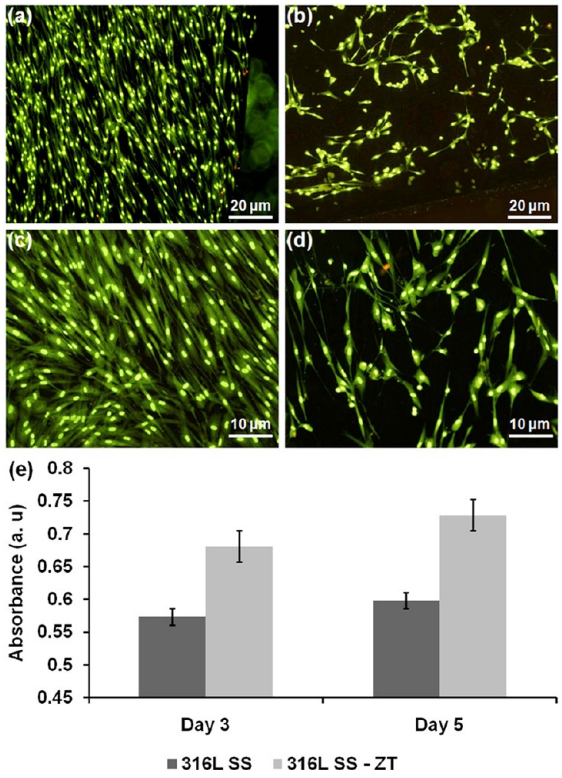

Figure 9. Fluorescence micrographs of live/dead staining of HDFn cells grown for 5 days on (a, b) bare 316 L SS and (c, d) ZT coated 316 L SS. (e) WST-1 proliferation assay demonstrating mitochondrial activity of HDFn cells after 3rd and 5th day of culture on implant materials.

samples. However, cell density obtained on day 3 over *ZT* coated 316 L SS samples shows significant ($p < 0.05$) increase in cell proliferation on day 5. WST-1 assay results showing high cell density over *ZT* coated 316 L SS samples on day 3 and day 5 finely coincides with live/dead staining images of Figure 9 c and d. These results elucidates that coating of *ZT* composites with porous morphology on 316 L SS facilitates the cellular attachment and therefore enhances the proliferation. Therefore, the biocompatibility of 316 L SS with *ZT* composite coating is comparatively higher than that of 316 L SS implant material.

4. CONCLUSIONS

The *ZT* nanocomposite was prepared by sol–gel method. The surface characterization studies revealed that the coated *ZT* nanocomposite exhibit polyphase and the coated film surface were uniform and porous. The in vitro characterization results indicated that the apatite growth exhibiting one-dimensional rod-like crystal on the coated surface after immersion in SBF solution for 7 days. Electrochemical characterization confirmed the lower passive current density and nobler corrosion potential for *ZT* nanocomposite compared to uncoated 316 L SS in SBF solution. The in vitro cell viability studies were performed on metal implants using human dermal fibroblasts culture and *ZT* composite coated 316 L SS metal implants showed high proliferation than uncoated metal implants. The above results indicated that the porous *ZT* nanocomposite coatings can be employed as a viable alternative in orthopedic applications to provide improved corrosion resistance and enhanced biocompatibility instead of the commercially available uncoated 316 L SS with numerous limitations in implant devices.

■ ASSOCIATED CONTENT

Ⓢ Supporting Information

SEM, EDS, water angle test, equivalent circuit for impedance analysis. This material is available free of charge via the Internet at http://pubs.acs.org/.

■ AUTHOR INFORMATION

Corresponding Author

*E-mail: nrajendran@annauniv.edu or vedichi@gmail.com.

Author Contributions

†These authors equally contributed to the research

Notes

The authors declare no competing financial interest.

■ ACKNOWLEDGMENTS

The corresponding author N.R. is grateful to All India Council for Technical Education (AICTE), New Delhi, India, for the financial assistance. In addition, this work is supported by WCU (World Class University) program through the National Research Foundation, Korea funded by the Ministry of Education, Science and Technology (R31-2008-000-10092).

■ REFERENCES

(1) Escalas, F.; Galante, J.; Rostoker, W.; Coogan, P. S. *J. Biomed. Mater. Res.* **1975**, *9*, 303–313.
(2) Walczak, J.; Shangalsi, F.; Heately, F. *Biomaterials* **1998**, *19*, 229–237.
(3) Carvalho, G. S.; Castanherira, M.; Digo, I. *J. Mater. Sci. Mater. Med.* **1995**, *7*, 777–783.
(4) Geesink, R. G. T. *Clin. Orthop.* **2002**, *395*, 53–65.
(5) Shirkhanzadeh, M. *J. Mater. Sci. Mater. Med.* **1998**, *9*, 67–72.
(6) Sridhar, T. M.; Kamachi Mudali, U.; Subbaiyan, M. *Corros. Sci.* **2003**, *45*, 237–252.
(7) Cotell, C. M. *Appl. Surf. Sci.* **1993**, *69*, 140–148.
(8) Bao, Q.; Chen, C.; Wang, D.; Ji, Q.; Lei, T. *Appl. Surf. Sci.* **2005**, *252*, 1538–1544.
(9) Wei, M.; Ruys, A. J.; Milthorpe, B. K.; Sorrell, C. C.; Evans, J. H. *J. Sol-Gel Sci. Technol.* **2001**, *21*, 39–48.
(10) Virtanen, S.; Milošev, I.; Gomez-Barrena, E.; Trebše, R.; Salo, J.; Konttinen, Y. T. *Acta Biomaterialia* **2008**, *4*, 468–476.
(11) Burdick, J. A.; Mauck, R. L. In *Biomaterials for Tissue Engineering Applications: A Review of the Past and Future Trends*, 1st ed.; Springer wien: New York, 2011; p 181.
(12) Gallardo, J.; Moreno, R.; Galliano, P.; Duran, A. *J. Sol–Gel Sci. Technol.* **2000**, *19*, 107–111.
(13) Sakk, S. *J. Sol–Gel Sci. Technol.* **1994**, *2*, 451–455.
(14) Guglielmi, M. *J. Sol–Gel Sci. Technol.* **1997**, *8*, 443–449.

(15) Keshmiri, M.; Troczynski, T. *J. Non-Cryst. Solids* **2003**, *324*, 289−294.
(16) Chen, D.; Jordan, E. H.; Gell, M.; Wei, M. *Acta Biomater.* **2008**, *4*, 553−559.
(17) Liu, J-X; Yang, D-Z; Shi, F; Cai, Y.-J. *Thin Solid Films* **2003**, *429*, 225−230.
(18) Kim, D-Y; Kim, M; Kim, H-E; Koh, Y-H; Kim, H-W; Jang, J.-H. *Acta Biomater.* **2009**, *5*, 2196−2205.
(19) Wang, N; Li, H; Lü, W; Li, J; Wang, J; Zhang, Z; Liu, Y. *Biomaterials* **2011**, *32*, 6900−6911.
(20) Paterson, M. J.; McCulloch, D. G.; Paterson, P. J. K.; Ben-Nissan, B. *Thin Solid Films* **1997**, *311*, 196−206.
(21) Balamurugan, A.; Kannan, S.; Rajeswari, S. *Mater. Lett.* **2003**, *57*, 4202−4205.
(22) Gallardo, J.; Galliano, P. *J. Sol−Gel Sci. Technol.* **2001**, *21*, 65−74.
(23) Miciukowicz, J.; Hang, T. *Appl. Catal., A* **1995**, *122*, 151−150.
(24) Liang, L.; Sheng, Y.; Xu, Y.; Wu, D.; Sun, Y. *Thin Solid Films* **2007**, *515*, 7765−7771.
(25) Ivanova, T.; Harizanova, A.; Koutzarova, T.; Krins, N.; Vertruyen, B. *Mater. Sci. Eng., B* **2009**, *165*, 212−216.
(26) Zhou, W.; Liu, K.; Fu, H.; Pan, K.; Zhang, L.; Wang, L.; Sun, C. C. *Nanotechnology* **2008**, *19*, 035610.
(27) Marchi, J.; Ussui, V.; Delfino, C. S.; Bressiani, A. H. A.; Marques, M. M. *J. Biomed. Mater. Res., Part B* **2010**, *94*, 305−311.
(28) Nagarajan, S.; Rajendran, N. *Appl. Surf. Sci.* **2009**, *15*, 3927−3932.
(29) Nagarajan, S.; Rajendran, N. *J. Sol−Gel Sci. Technol.* **2009**, *52*, 188−196.
(30) Kokubo, T.; Takadama, H. *Biomaterials* **2006**, *27*, 2907−2915.
(31) Bard, A. J; Faulkner, L. R. In *Electrochemical Methods: Fundamentals & Applications*, 2nd ed.; John Wiley & Sons: New York, 1980; p 103.
(32) Teufer, G. *Acta Crystallogr.* **1962**, *15*, 1187.
(33) Cueto, L. F.; Sánchez, E.; Torres-Martinez, L. M.; Hirata, G. A. *Mater. Charact.* **2005**, *55*, 263−271.
(34) Sekulic, J.; Magraso, A.; Ten Elshof, J. E.; Blank, D. H. *Microporous Mesoporous Mater.* **2004**, *72*, 49−57.
(35) Kim, H. M.; Kokubo, T.; Fujibayashi, S.; Nishiguchi, S.; Nakamura, T. *J. Biomed. Mater. Res., Part A* **2000**, *52*, 553−557.
(36) Kunze, J.; Muller, L.; Macak, J. M.; Greil, P.; Schmuki, P.; Muller, F. A. *Electrochim. Acta* **2008**, *53*, 6995−7003.
(37) Panda, R. N.; Hsieh, M. F.; Chung, R. J.; Chin, T. S. *J. Phys. Chem. Solids.* **2003**, *64*, 193−197.
(38) Yu, J. C.; Yu, J.; Tang, H. Y.; Zhang, L. *J. Mater. Chem.* **2002**, *12*, 81−85.
(39) Raman, V.; Tamilselvi, S.; Rajendran, N. *Electrochim. Acta* **2007**, *52*, 7418−7424.
(40) Gonzalez-Mcquire, R.; Chane-Ching, J. Y.; Vignaud, E.; Lebugle, A.; Mann, S. *J. Mater. Chem.* **2004**, *14*, 2277−2281.
(41) Liu, Y.; Hou, D.; Wang, G. *Mater. Chem. Phys.* **2004**, *86*, 69−72.
(42) Bou-Saleh, Z.; Shahryari, A.; Omanovic, S. *Thin Solid Films* **2007**, *515*, 4727−4737.
(43) Souto, R. M.; Laz, M. M.; Reis, R. L. *Biomaterials* **2003**, *24*, 4213−4221.